



PERGAMON

*Acta mater.* Vol. 47, No. 12, pp. 3515–3532, 1999  
© 1999 Acta Metallurgica Inc.  
Published by Elsevier Science Ltd. All rights reserved  
Printed in Great Britain  
1359-6454/99 \$20.00 + 0.00

PII: S1359-6454(99)00148-2

## AN EXPERIMENTAL–COMPUTATIONAL APPROACH TO THE INVESTIGATION OF DAMAGE EVOLUTION IN DISCONTINUOUSLY REINFORCED ALUMINUM MATRIX COMPOSITE

M. LI<sup>1</sup>, S. GHOSH<sup>1†</sup> and O. RICHMOND<sup>2</sup>

<sup>1</sup>Department of Aerospace Engineering, Applied Mechanics and Aviation, The Ohio State University, Columbus, OH 43210, U.S.A. and <sup>2</sup>ALCOA Technical Center, ALCOA Center, PA 15069, U.S.A.

(Received 8 January 1999; accepted 23 April 1999)

**Abstract**—A combined experimental–computational approach to study the evolution of microscopic damage to cause failure in commercial SiC particle reinforced DRAs is dealt with. Determination of aspects of microstructural geometry that are most critical for damage nucleation and evolution forms a motivation for this work. An interrupted testing technique is invoked where the load is halted in the material instability zone, following necking but prior to fracture. Sample microstructures in the severely necked region are microscopically examined in three dimensions using a serial sectioning method. The micrographs are then stacked sequentially on a computer to reconstruct three-dimensional microstructures. Computer simulated equivalent microstructures with elliptical or ellipsoidal particles and cracks are constructed for enhanced efficiency, which are followed by tessellation into meshes of two- and three-dimensional Voronoi cells. Various characterization functions of geometric parameters are generated and sensitivity analysis is conducted to explore the influence of morphological parameters on damage. Micro-mechanical modeling of two-dimensional micrographs are conducted with the Voronoi cell finite element method (VCFEM). Inferences on the initiation and propagation of damage are made from the two-dimensional simulations. Finally, the effect of size and characteristic lengths of representative material element (RME) on the extent of damage in the model systems is investigated. © 1999 Acta Metallurgica Inc. Published by Elsevier Science Ltd. All rights reserved.

**Key words:** Computer simulation; Image analysis; Aluminum composites; Microstructure; Fracture and Fracture toughness

### 1. INTRODUCTION

The commercial use of particle-reinforced metal matrix composites in automotive, aerospace and other engineering systems has increased in the last few decades due to their potentially superior mechanical properties, as well as their ability to reduce life-cycle costs through enhanced thermal stability and weight reduction. The property advantages of these materials are, however, often diminished by general degradation of failure properties like ductility and fracture toughness. Various experimental and numerical studies [1–10] have been conducted to understand the influence of morphological factors such as volume fraction, size, shape and spatial distribution as well as constituent material and interface properties on the deformation and damage behavior. These studies have concluded that failure mechanisms are highly sensitive to local reinforcement distribution, morphology, size, interfacial strength, etc.

Traditionally *unit cell* models [11–15] based on the finite element analysis have been used to predict the onset and growth of evolving damage in composite materials. While these models provide valuable insights into the microstructural damage processes, simple morphologies idealize actual microstructures for many engineering materials that bear little relationship to the actual stereographic features. These deficiencies have been circumvented in Refs [8, 16, 17], where computational models of discontinuously reinforced materials with random spatial dispersion have been considered. Richmond and co-workers [18, 19] have investigated the effect of morphology on damage in composite, porous and polycrystalline materials by modeling actual geometries obtained from two-dimensional micrographs. Using the Voronoi cell finite element model, Moorthy and Ghosh [10, 11] have examined the effect of various spatial dispersions and particle shape and size on the damage initiation and evolution process in ductile matrix composites.

Many characterization studies with two-dimensional microstructures, e.g. Refs [19–22], have also

†To whom all correspondence should be addressed.

been conducted to understand the relation between microstructural morphology and damage. Experimental research [23–27] has however pointed to the necessity of examining the full three-dimensional characteristics for understanding the damage process. These studies infer that two-dimensional assessment can sometimes be misleading, especially in the presence of spatial clustering. Non-destructive evaluation methods, e.g. techniques based on ultrasonics, e.g. Ref. [28], acoustic emission [4] and X-ray based computer tomography (CT) [29, 30] have emerged as potential methods for studying three-dimensional damage. However, many of these systems are thus far not capable of achieving spatial resolutions required to accurately capture microscopic particles and damage in the particle reinforced MMCs. Buffiere *et al.* [31] are developing a CT technology to yield tomographic images with a higher spatial resolution.

This paper deals with a combined experimental–computational approach to study the evolution of microscopic damage to cause complete material failure in commercial SiC particle reinforced aluminum alloys or DRAs. Through a combination of two- and three-dimensional characterization and analysis models, it is intended to understand which aspects of microstructural morphology are most critical for damage nucleation and evolution. Since it is difficult to identify the microcrack growth process once a material has failed completely, an interrupted testing technique is designed. Subsequently, sample microstructures in the severely necked region are microscopically examined in three dimensions using a serial sectioning method discussed in Refs [23, 24, 32]. Computer simulated equivalent microstructures are tessellated into meshes of two- and three-dimensional Voronoi cells. Various characterization functions of geometric parameters are generated and a sensitivity analysis is conducted to explore the influence of morphological parameters on damage. Two-dimensional characterization functions are compared with three-dimensional ones to evaluate the effectiveness of modeling the two-dimensional micrographs. Modeling of the initiation and propagation of damage is conducted with the Voronoi cell finite element method (VCFEM) [9, 10, 31, 33]. Each Voronoi cell element may consist of a matrix phase, an inclusion phase and a crack phase. Damage initiation by particle cracking is assumed to follow a maximum principal stress based Rankine criterion. The VCFEM for particle cracking has shown a significant promise in modeling large aggregates of heterogeneities. While the appropriateness of three-dimensional analyses is recognized for this study, the three-dimensional VCFEM (under development) does not currently have all the necessary features. Due to enormous computing requirements of conventional three-dimensional FEM models, various studies have resorted to simplified manifestations of

complex geometries and properties, e.g. Refs [7, 15, 34]. This study is restricted to two dimensions in the form of VCFEM analyses of section micrographs. Finally, the effect of size and characteristic lengths of representative material element (RME) on the extent of damage in the model systems is also investigated.

## 2. EXPERIMENTS FOR DAMAGE ASSESSMENT

### 2.1. Interrupted tests

The material analyzed in this work is a discretely reinforced commercial aluminum that is fabricated by a powder metallurgy process [35]. It consists of extruded commercial X2080 aluminum alloy with 15% volume fraction SiC particles. The X2080 matrix has a nominal alloy composition with weight percentages of 3.8% Cu, 1.8% Mg and 0.2% Zr, in addition to low impurity contents of Fe and Si. The precipitation hardened X2080 aluminum alloy system is naturally aged by heat treating for 4 h at 930°F, followed by cold water quench and aging for 2 days at room temperature.

An important object in this failure study is to obtain adequate microstructural data that depict the growth of damage into a major failure path. In general, it is difficult to identify the dominant damage mechanisms and also the microcrack growth process, once a material has fractured completely. Thus an interrupted testing technique is designed where the load and deformation are halted in the material instability zone, following necking but prior to fracture. The tests assume that the major cracks are essentially prominent at this stage, and are helpful in understanding the linkage mechanism of microcracks or particle debonds to facilitate growth of the dominant damage. To initialize the testing, estimates of the necking and fracture strains are first obtained by observing the behavior of a tension test to failure. The uniaxial tension tests are executed on an MTS 810 material system with a HP 7044 X–Y recorder to monitor the loads and strains, and the critical strains are measured with an MTS 632.11 strain gauge extensometer. Following the initialization, strain controlled interrupted tests are carried out, in which the specimens are loaded to the instability region before the load is stopped.

Figure 1(a) shows a typical tension specimen for the naturally aged material. Data for six specimens of this material, namely t1, t2, t3, t4, t5 and t6 are tabulated in Table 1. The specimens t1, t2, t4 and t6 are obtained from the outer annulus region of the stock material while t3 and t5 are from the central core regions. The initialization of the test to study the entire material behavior and estimate the post-instability region is done with specimens t1 and t2. The material load–displacement curve is plotted in Fig. 1(b), from which the necking strain

is obtained from the peak load value. For the specimen t1, the test is conducted at a strain rate of  $\dot{\epsilon} = 5 \times 10^{-4}/s$  and the necking strain and fracture strain are found to be  $\epsilon_n = 9.15\%$  and  $\epsilon_f = 9.40\%$ , respectively. The short instability region in t1 prompts a reduced strain rate  $\dot{\epsilon} = 3 \times 10^{-4}/s$  for specimen t2, for which  $\epsilon_n = 9.05\%$  and  $\epsilon_f = 9.20\%$ .

In Table 1,  $\dot{\epsilon}$ ,  $\epsilon_n$  and  $\epsilon_f$  correspond to the strain rate, the necking strain and the interrupted strain, respectively. The interrupted strain coincides with the fracture strain in the event that fracture precedes the load stoppage. This is indicated with F or I in the table. Load interruption is only possible for specimens t3 and t6 due to the extremely short

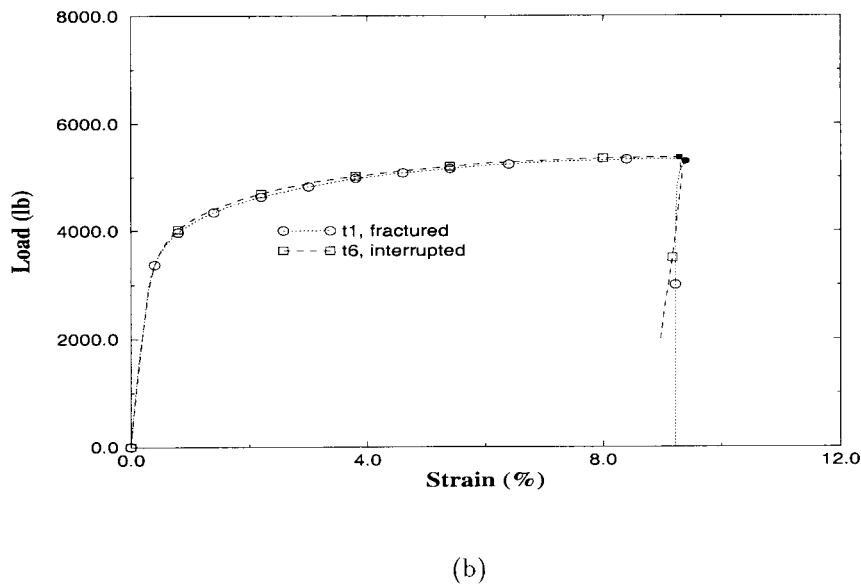
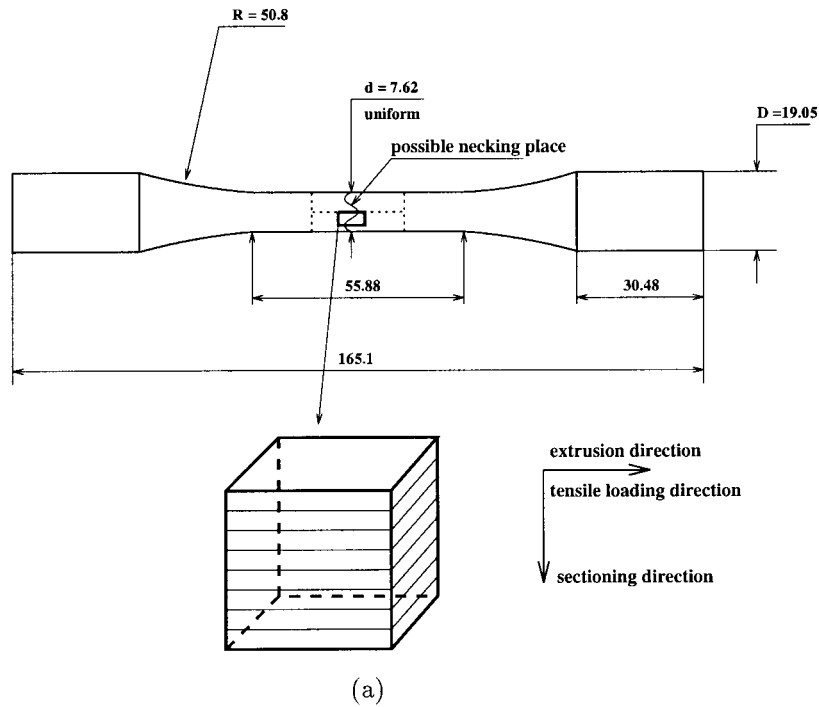


Fig. 1. (a) Interrupted uniaxial tensile test specimen for naturally aged material and sample coupon for serial sectioning (unit in mm). (b) Load-strain plots for two specimens of naturally aged DRA. Dark points indicate where the loading is interrupted or where the specimen is fractured.

post-instability range of this material in comparison with the resolution of the loading mechanism. The necking strains for the specimens t1, t2, t4 and t6 are in the range of 9.00–9.30%, while those for specimens t3 and t5 are in the 9.80–10.20% range. This difference is possibly due to gradients created by the heat treatment at different locations in the stock material. The core cools slower and more uniformly regions near the surface. This results in the more uniform microstructure and larger necking and fracture strains for specimens (t3 and t5) located near the core of the stock material.

## 2.2. Damage examination and microscopic analysis

To examine the dependence of microstructural damage on the local morphology, serial sectioning of sample coupons extracted from the load-interrupted specimens t3 and t6, is invoked. This method, discussed in Refs [23, 24, 32], involves gradual removal of material layers to obtain a series of scanning electron/optical micrographs, representing sections of a microstructure. It is a very effective method for reconstructing three-dimensional microstructures from a series of two-dimensional sections of particulate reinforced composites, requiring a resolution of a few microns. Prior to sectioning, locations are selected in Fig. 1(a) for cutting out the sample coupons. X-rays and acoustic microscopy with an AEROTECH UNIDEX 11 acoustic microscope with a resolution of about  $50\ \mu\text{m}$  are used in this process to detect regions that contain major crack paths. Polished surfaces of these extracted samples are then examined by a Nikon optical microscope for major damage sites. For specimen t3, shorter cracks passing through two to three particles at most are found. However, for specimen t6, a larger crack passing through five to six particles is identified, and is consequently chosen for analysis in this paper. Coupons of approximate size  $6 \times 6 \times 6\ \text{mm}^3$  are subsequently prepared for the serial sectioning operation to sequentially expose parallel sections of the microstructure. As discussed in Refs [23, 24, 32], parallel layers in a direction perpendicular to the straining direction [see Fig. 1(a)] are removed using a precision dimple grinder. The depth of material removal per step is selected such that each particle is sectioned at least once, ensuring that all particles of interest are adequately captured in the micrographs. For the DRA considered, the

particle size range is approximately  $3\text{--}25\ \mu\text{m}$ , with an average size of  $\sim 9.2\ \mu\text{m}$  and the standard deviation is  $3.891\ \mu\text{m}$ . The section to section step size is chosen to be  $2\ \mu\text{m}$ , corresponding to a total traversed thickness of  $36\ \mu\text{m}$  for 18 sections. Two typical micrographs showing damage are depicted in Fig. 2, for which the horizontal corresponds to the loading direction. The micrographs are then serially stacked using graphics software [36] to yield three-dimensional microstructures as shown in Fig. 3(a). The precise three-dimensional location, shape, size and orientation of each particle can be obtained at a fairly high resolution by this method.

## 2.3. Major observations

The micrographs of serial sections 3 and 5 in Fig. 2, perpendicular to the middle plane of the tensile specimen, provide important information on the evolution of the dominant damage path in the material. A dominant damage path is clearly seen in the boxed regions. The damage size progressively diminishes with increasing sections, indicating the end of the cracked particles. The particle area fraction (AF), total number of particles (NP) and total number of cracked particles (NCP) for each section micrograph are presented in Table 2. Generally speaking, sections with large AF and NCP are found to contain the larger cracks. The three-dimensional image by assembling two-dimensional micrographs in Fig. 3(a) also shows the dominant damage path in the boxed region.

From the microscopic observation results, it is found that for the naturally aged material, the main mode of damage is by particle cracking. Large particles in particle rich regions are more susceptible to cracking than those in particle sparse regions. Microcracks in the particle rich areas link up to form paths of dominant damage. The linkage and evolution of these larger cracks lead to the overall failure of the material. These paths are approximately perpendicular to the tensile loading direction. Thus, spatial distribution of particles plays a more important role in damage than particle size for this material.

## 3. EQUIVALENT MICROSTRUCTURE AND MESH GENERATION

The actual three-dimensional geometry of particles, as seen in Fig. 3(a), can be quite complex

Table 1. Naturally aged material interrupted tensile test results:  $\dot{\epsilon}$  is the strain rate,  $\epsilon_n$  and  $\epsilon_i$  are the necking strain and interrupted strain. F or I indicates whether the specimen is fractured or the test is interrupted

SP	$\dot{\epsilon}$ ( $10^{-4}$ /s)	$\epsilon_n$ (%)	$\epsilon_i$ (%)	F(I)	$\Delta_\epsilon$ (%)
t1	5	9.15	9.40	F	0.25
t2	3	9.05	9.20	F	0.15
t3	3	10.20	10.37	I	0.17
t4	2	9.30	9.40	F	0.10
t5	2	9.80	10.33	F	0.53
t6	2	8.80	9.29	I	0.49

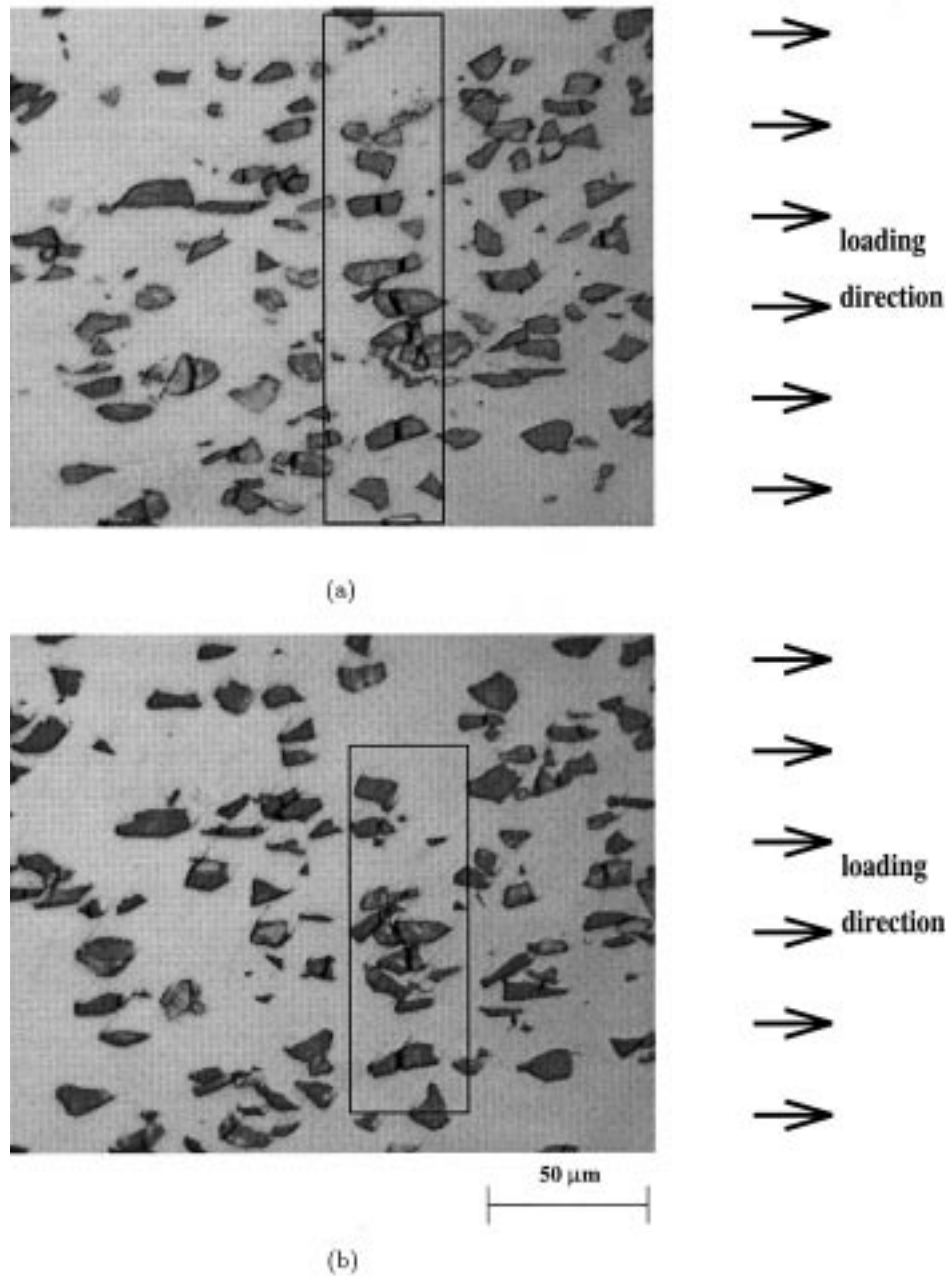


Fig. 2. Micrographs of different sections of the t6 specimen showing cracked particles: (a) section 3; (b) section 5.

and an exhaustive database is required to store all geometric details. To avert this, equivalent microstructures that closely approximate the actual morphology but are computationally less demanding, are generated. In this process, each particle and an associated crack are replaced by equivalent ellipses (in two dimensions) or ellipsoids (in three dimensions). This method economizes the image analysis and characterization process by way of well-known geometric properties. To obtain equivalent microstructures, digitized image data are first transferred into a binary format to distinguish between the par-

ticle, matrix and crack phases. The zeroth ( $I_0$ ), first ( $I_x, I_y$ ) and second ( $I_{xx}, I_{yy}$ ) order geometric moments are then computed for each particle by adding contributions from each voxel (in three dimensions) or pixel (in two dimensions) that lies within the particle boundary. For two-dimensional microstructures the computed moments are equated to the moment formulae for ellipses to evaluate the centroidal coordinates ( $x_c, y_c$ ), half major and minor axis lengths ( $a, b$ ), and orientation  $\theta$  of the major axis from:

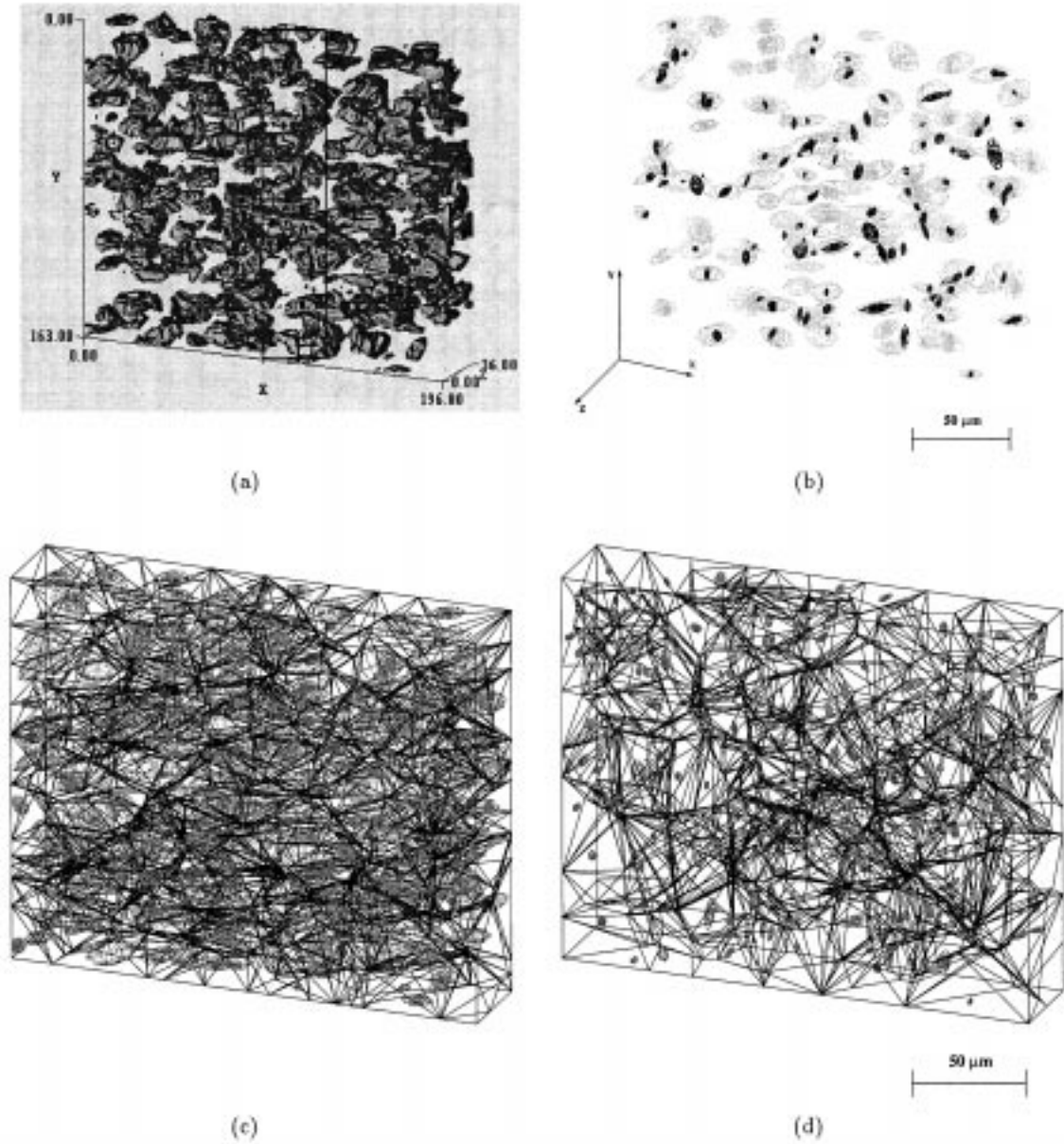


Fig. 3. Three-dimensional microstructure for SiC particle reinforced DRA after interrupted test (units in  $\mu\text{m}$ ): (a) a computer created image by serially stacking section micrographs; (b) simulated microstructure of ellipsoidal particles and cracks. Tessellation for two- and three-dimensional microstructures: (c) three-dimensional tessellation based on particle morphology; (d) three-dimensional tessellation based on microcrack morphology.

$$\begin{aligned}
 x_c &= \frac{I_y}{I_0}, \quad y_c = \frac{I_x}{I_0}, \quad a \\
 &= \sqrt{\frac{1}{2}(C_1 + \sqrt{C_1^2 - 4C_2})}, \quad b \\
 &= \sqrt{\frac{1}{2}(C_1 - \sqrt{C_1^2 - 4C_2})}, \quad \theta \\
 &= \frac{1}{2} \cos^{-1} \left( \frac{4}{a^2 - b^2} \right) \left( \frac{I_{yy} - I_{xx}}{I_0} - \frac{I_y^2 - I_x^2}{I_0^2} \right) \quad (1)
 \end{aligned}$$

where

$$C_1 = 4 \left( \frac{I_{xx} + I_{yy}}{I_0} - \frac{I_x^2 + I_y^2}{I_0^2} \right)$$

and  $C_2 = I_0^2/\pi^2$ . For three-dimensional microstructures, the centroidal coordinates ( $x_c, y_c, z_c$ ) of the equivalent ellipsoid are first evaluated from the zeroth and first order moments as:  $x_c = I_y/I_0$ ,  $y_c = I_x/I_0$ ,  $z_c = I_z/I_0$ . The principal directions (or orientations of the three axes) for the ellipsoids are

Table 2. Experimental observations of particle area fraction (AF), total number of particles (NP) and total number of cracked particles (NCP) for different sections of specimen t6

Section #	1	2	3	4	5	6	7	8	9	10	11	13	14	16	18
AF (%)	18	20	19	20	19	19	19	19	17	16	16	16	15	17	17
NP	105	107	120	118	113	110	99	105	110	115	116	116	105	106	104
NCP	33	34	33	30	29	25	24	26	24	27	29	34	30	24	26

obtained from the eigenvalues of the second order moments  $I_{ij}$  ( $i = 1, \dots, 3, j = 1, \dots, 3$ ). The major (2a), intermediate (2b) and minor (2c) axes of the equivalent ellipsoids are then obtained from the principal moments  $I_1, I_2, I_3$  as

$$\begin{aligned} a &= \sqrt{\frac{5}{I_0}(I_2 + I_3 - I_1)}, \quad b = \sqrt{\frac{5}{I_0}(I_1 + I_3 - I_2)}, \\ c &= \sqrt{\frac{5}{I_0}(I_1 + I_2 - I_3)}. \end{aligned} \quad (2)$$

A simulated three-dimensional microstructure with particles (grey) and cracks (black) is shown in Fig. 3(d). The microstructures are then tessellated into a mesh of two- and three-dimensional Voronoi cells, by surface based algorithms detailed in Refs [23,24]. In Fig. 3(c), the mesh of Voronoi cells is created based on the morphology of particles, while in Fig. 3(d) the mesh is due to tessellation based on the geometry of particle cracks. Tessellation into a mesh of Voronoi cells plays an important role in developing geometric descriptors for quantitative characterization. They represent regions of immediate influence for each heterogeneity and also define the neighbor of each heterogeneity from individual faces or edges of the Voronoi cells. This facilitates easy evaluation of parameters like local area fractions, near neighbor and nearest neighbor distances and orientations.

#### 4. MICROSTRUCTURE AND DAMAGE CHARACTERIZATION

The morphology of particles and associated damage or microcracks can be characterized by various functions of size, shape, orientation and spatial distribution. A number of these classifier functions have been used by the authors and others in Refs [6, 19–21, 23, 24, 31–33] to characterize various aspects of microstructural morphology. In this section, some of these functions are considered for the three-dimensional microstructure and two-dimensional micrographs to investigate the relation between morphological characteristics and the path of dominant damage in the material. The specimen t6 with a large microcrack is considered for this study.

In the first exercise, a sensitivity analysis is done with the simulated three-dimensional microstructure in Fig. 3(b) to reveal the dependence of damage on microstructural variables. Two damage parameters, namely the number fraction of cracked particles (**nf**)

and the volume fraction of cracked particles (**vf**) are chosen to manifest the damage level in the DRA. Six microstructural parameters are considered, namely (i) particle equivalent size (diameter); (ii) nearest neighbor distance computed as the distance between particles that share a common Voronoi cell edge; (iii) local volume fraction measured as a ratio of the particle size to that of the associated Voronoi cell; (iv) particle shape or ellipsoid aspect ratio; (v) nearest neighbor orientation, measured as the angle between a line joining the centers of a particle and its nearest neighbor, and the loading direction; and (vi) particle orientation with respect to the loading direction. The cracked particle fractions are plotted as functions of these parameters in Fig. 4. A linear interpolation, obtained by a least square fit, yields the corresponding overall gradient or slope.

While both the **nf** and **vf** plots coincide for the particle size plot (i), large differences are noted for nearest neighbor distances (ii) and aspect ratios (iv). Largest slopes of these plots are observed with particle size, nearest neighbor distance and local volume fraction. This infers that the strongest influence on particle cracking comes from the size and local spatial distribution. Particle shape has a relatively smaller effect on damage initiation. Sensitivity of damage to particle orientation and nearest neighbor orientation is found to be minimal for this material.

The characteristics of particles forming the dominant damage path [within the marked box in Fig. 3(a)] are compared with those for all cracked particles in the histograms of Fig. 5. The dotted lines correspond to all cracked particles while the shaded areas are for cracked particles in the dominant damage region only. The histograms are with respect to three variables that are found to play important roles in the damage process, namely the particle size, nearest neighbor distance and orientation with respect to the loading direction. While the range of sizes for all cracked particles is 4–13  $\mu\text{m}$ , that for the particles forming the dominant damage path is 5.7–13  $\mu\text{m}$ . This reveals that larger particles generally contribute to the dominant damage path. The plot of the nearest neighbor clearly exhibits the influence of particle rich areas (clustering or alignment) on the preferential growth of damage. The nearest neighbor distance for particles in the dominant damage path is in the range 0.4–3.7  $\mu\text{m}$  when compared with the range 0.4–12.3  $\mu\text{m}$  for all cracked particles. The histogram of

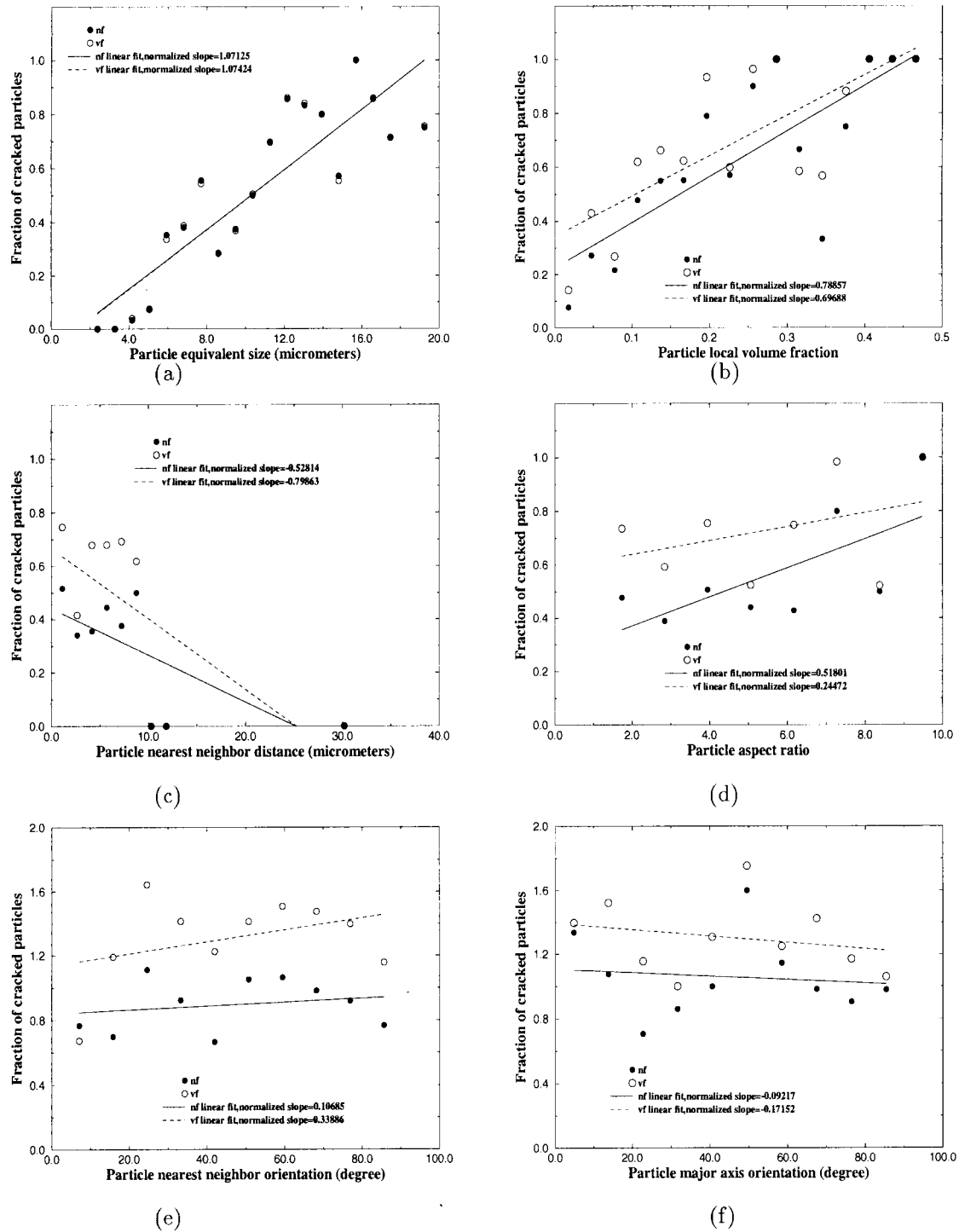
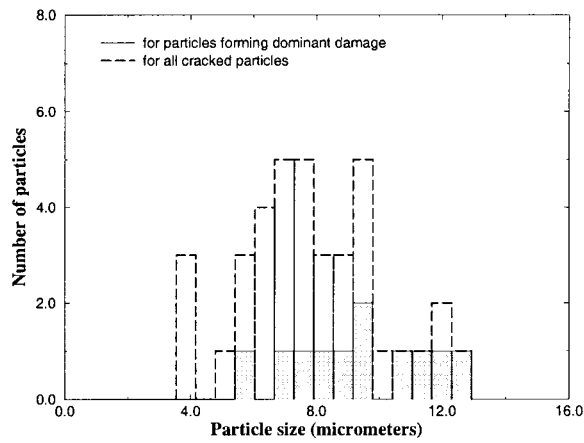


Fig. 4. Sensitivity of damage to various microstructural variables.

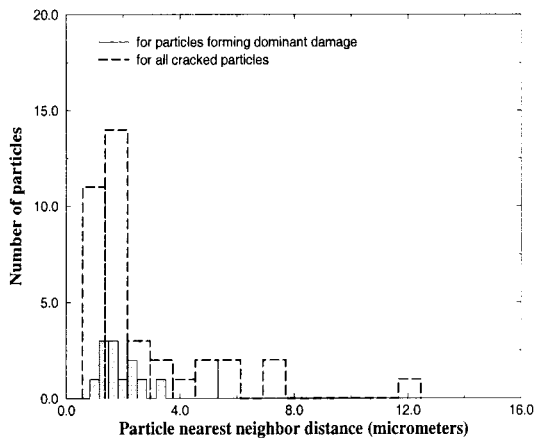
cracked particles as a function of the orientation with respect to the loading direction reveals that particles with major axis along the loading direction ( $0^\circ$  and  $180^\circ$ ) are generally susceptible to cracking. This is much more pervasive for particles in the dominant damage path, due to the smaller cross-

sectional areas normal to loading. In conclusion, particles in the dominant damage path generally have larger size, are in particle rich areas, and are oriented in the loading direction.

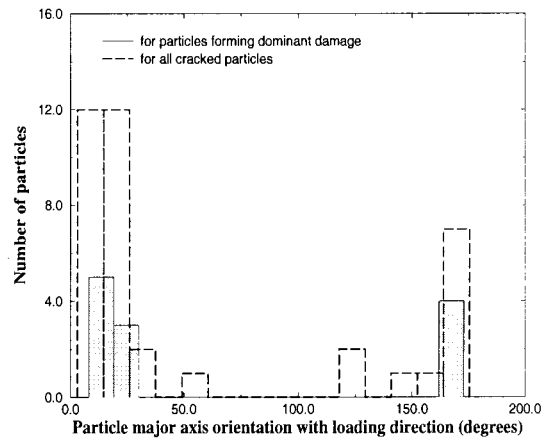
Finally, it is of interest to identify discriminating characteristics of two-dimensional micrographs that



(a)



(b)



(c)

Fig. 5. Histograms comparing characteristics of particles with dominant damage with all cracked particles.

may be helpful in making dominant damage predictions for the actual three-dimensional microstructures. Two representative micrographs, namely section 1 which contains a dominant damage and section 14 without any dominant damage, but only scattered particle cracks are compared with the three-dimensional microregion. Four important characterization functions, namely (a) the probability density function of particle equivalent size (diameter), (b) the probability density function of the nearest neighbor distance, (c) the probability density function of the local area/volume fraction and (d) a transformation function  $L(r)$  of a second order intensity function  $K(r)$ , are plotted in Fig. 6

for two- and three-dimensional micrographs. The second order intensity function  $K(r)$  and its transformed functions  $[L(r) = (K(r)/\pi)^{1/2}]$  in two dimensions, and  $L(r) = ((3/4\pi)K(r))^{1/3}$  in three dimensions) which capture second order statistics of spatial distributions are used as a graphical tool for detecting departures from a homogeneous Poisson process [23, 24, 31, 33]. The plot of  $L(r)$  vs  $r$  is a 45° straight line for a pure Poisson distribution.

The plots distinctly reveal a few important features of the micrographs. The particle size distribution for the two two-dimensional micrographs are similar and the tails are significantly shorter than three-dimensional ones. As is expected, three-

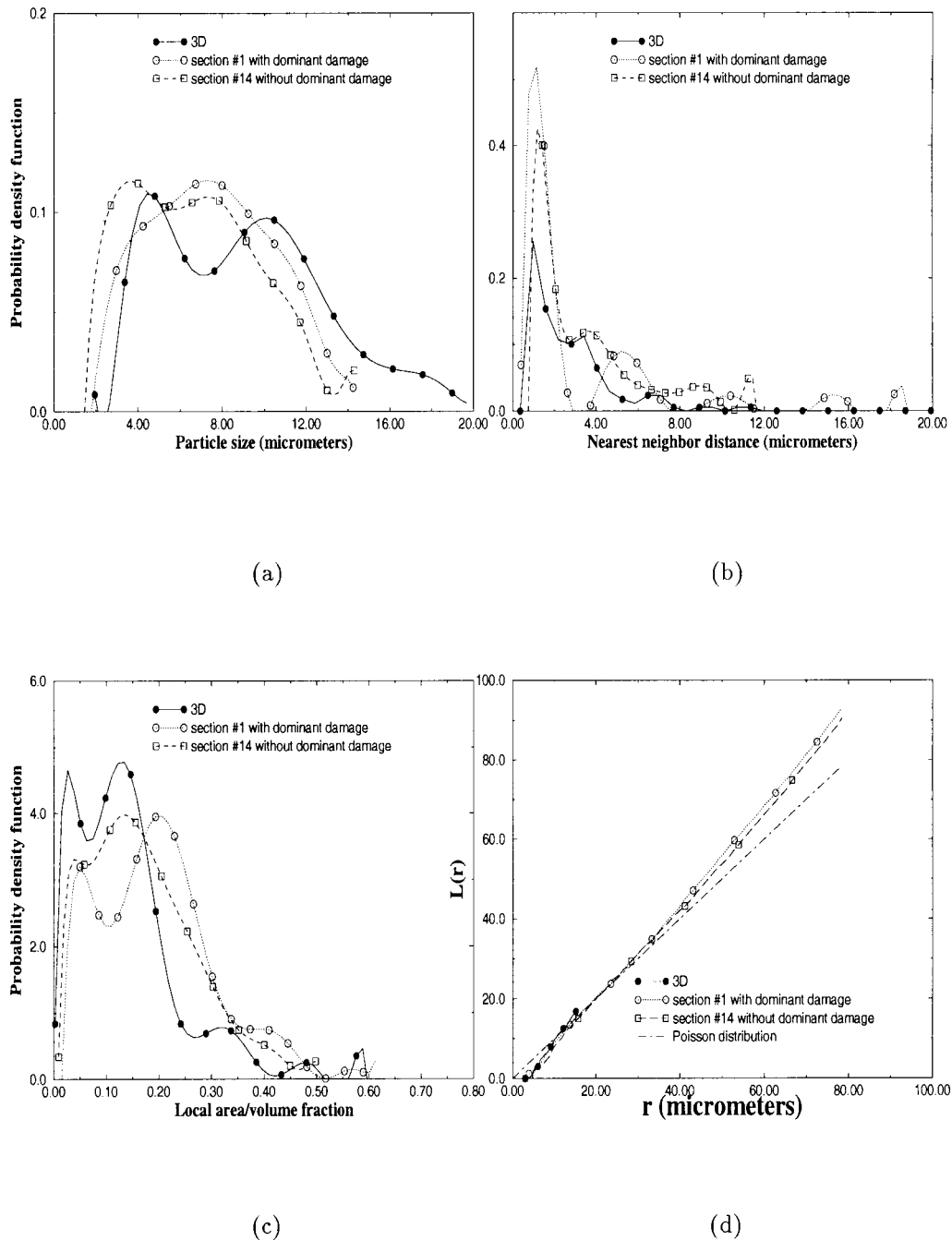


Fig. 6. Characterization functions for two-dimensional sections and three-dimensional microstructure.

dimensional particle sizes are larger than two-dimensional particle section sizes due to sectioning along non-principal planes. However, the probabilities of both the nearest neighbor distances and local area fractions in Figs 6(b) and (c) yield a distinguishing characteristic. The micrograph with dominant damage has peaks and valleys, as well as tails that are very similar to that for three dimensions. The peaks which reflect particle rich regions

and the tails which reflect sparse areas are both found to be important discriminants. Deviation from the  $L(r) = r$  function or the  $45^\circ$  line represents a bias towards clustering. The section with the dominant damage has a larger deviation from the random distribution in comparison with the section without major cracking, and is closer to the three-dimensional response. In summary, it may be concluded that when analyzing two-dimensional sec-

tions, the likelihood of better representation of dominant damage is for those sections that have higher peaks at lower nearest neighbor distances with longer tails and have higher deviation from the Poisson distribution. Similar observations have also been made in Refs [1, 5, 27, 37].

**5. DAMAGE SIMULATION BY VORONOI CELL FEM**

Two-dimensional plane strain/stress simulations of the microstructural damage evolution is conducted by the Voronoi cell finite element model (VCFEM) described in Refs [9, 10, 31, 33]. The current two-dimensional VCFEM only accommodates particle cracking, and hence matrix cracking is ignored in the simulations. The simulations are useful in understanding the damage evolution process by a sequence of particle cracking. Rectangular  $195 \times 155.018 \mu\text{m}^2$  micrographs as shown in Figs 8(a) and (b) are analyzed with monotonically increasing strains. Periodicity boundary conditions are imposed by requiring edges to remain straight and parallel to the original direction throughout deformation as

$$\begin{aligned} u_x &= 0 \text{ (on } x = 0), u_y = 0 \text{ (on } y = 0), u_x \\ &= u_{ap} \text{ (on } x = L_x), u_y = D_y^* \text{ (on } y = L_y), T_y \\ &= 0 \text{ (on } x = 0/L_x), T_x = 0 \text{ (on } y = 0/L_y) \end{aligned} \quad (3)$$

where  $u_{ap}$  is an applied displacement and  $D_y^*$  is determined from the average force condition  $\int_X T_x dx = 0$  on  $y = L_y$ . The reinforcing phase of SiC particles is assumed to be brittle and is modeled with the linear elastic properties: Young’s modulus  $E = 427 \text{ GPa}$ , Poisson’s ratio  $\nu = 0.17$ . The aluminum matrix material is assumed to be ductile and is modeled by small deformation isotropic hardening  $J_2$  elasto-plasticity theory with properties: Young’s modulus  $E = 72 \text{ GPa}$ , Poisson’s ratio  $\nu = 0.33$  and the post yield elastic-plastic behavior is obtained from Ref. [38] as shown in Fig. 7. Microstructural damage by particle cracking is assumed to be governed by a maximum principal stress or Rankine criterion. In this criterion, a crack is initiated when the maximum principal stress in tension exceeds a critical fracture stress  $\sigma_{cr}$  at a point. The crack is

oriented at right angles to the principal stress direction. The critical stress  $\sigma_{cr}$  is also influenced by the particle size due to the existence of microcracks. To account for the size effect in  $\sigma_{cr}$ , a Weibull distribution based criterion is used, where the probability of particle fracture  $P_f(A, \sigma)$  is related to the particle volume/area  $v$  and the maximum principal stress  $\sigma_1$  as

$$P_f(v, \sigma_1) = 1 - \exp\left[-v\left(\frac{\sigma_1}{\sigma_0}\right)^m\right] \quad (4)$$

where  $\sigma_0$  and  $m$  are two material parameters in the Weibull distribution that are calibrated from experiments.

*5.1. Calibration of Weibull parameters  $\sigma_0$  and  $m$*

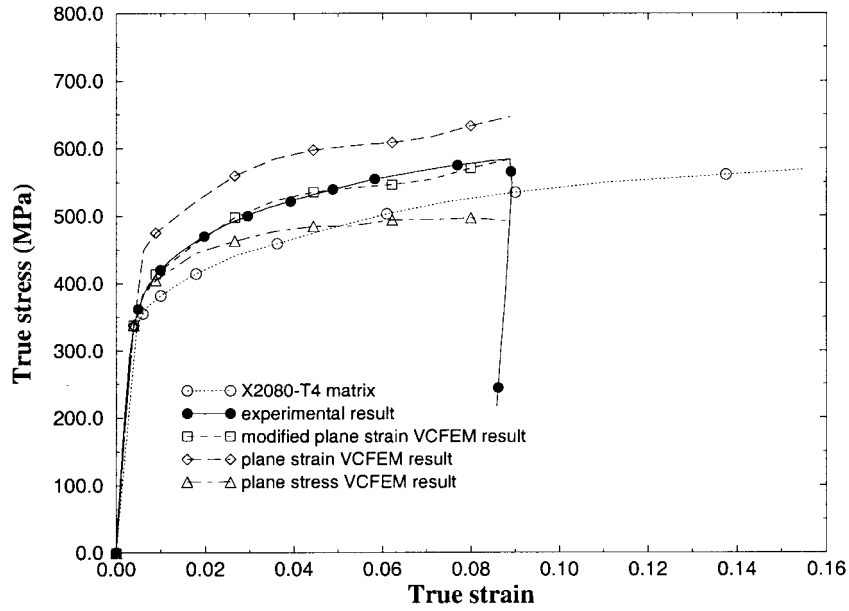
In the two-parameter Weibull model, the fraction of fractured particles may be obtained [24, 34, 39] from a known probability distribution of particle volumes  $p(v)$ , as

$$\begin{aligned} \rho(v) &= \int_{V_{min}}^{V_{max}} p(v)P_f(v, \sigma_1) dv \approx \sum_{i=1}^N p(v_i) \\ &\times \left(1 - \exp\left[-\frac{v_i}{v_0}\left(\frac{\sigma_1^i}{\sigma_0/v_0}\right)^m\right]\right) \Delta v_i \end{aligned} \quad (5)$$

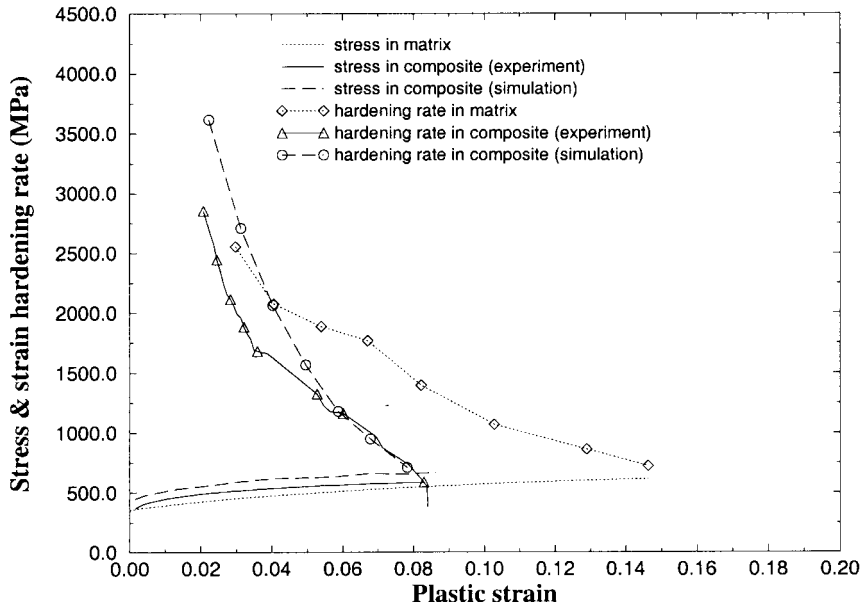
where  $p(v_i)$  is the probability density distribution of particle volume/area  $v_i$ . The entire area is divided into  $N$  intervals such that  $\Delta v_i = v_i - v_{i-1}$ ,  $\sigma_1^i$  is the average particle maximum principal stress for particles with size in the range of  $[v_{i-1}, v_i]$  and  $v_0$  is a reference area taken to be the average area. The fraction of cracked particles  $\rho$  is readily obtained from the experimental micrographs. Again, the section micrographs 2, 8 and 14 are used to calibrate the Weibull parameters. The fractions of cracked particles and the average particle area for these three sections are 31.78, 24.76, 28.57% and 53.43, 48.91, 52.67  $\mu\text{m}^2$ , respectively. The maximum principal stress  $\sigma_1^i$  for each particle is obtained from VCFEM simulation prior to the onset of particle cracking at a true strain of  $\epsilon = 8.88\%$ . From the experimental observations it is assumed that no major damage has been initiated at this strain. The Weibull parameter  $m$  is assumed to take integer values between 1 and 8 following Refs [24, 39] and the corresponding values of  $\sigma_0$  are given in Table 3.

Table 3. Calibration of Weibull parameter  $\sigma_0$  (GPa)

$m$	Section #2	Section #8	Section #14	Three-dimensional (without shape)	Three-dimensional (with shape)
1	111.91	119.80	96.84	296.82	308.12
2	10.55	11.05	9.41	16.00	16.30
3	4.80	5.01	4.34	6.04	6.12
4	3.22	3.38	2.95	3.72	3.75
5	2.53	2.67	2.34	2.77	2.80
6	2.15	2.28	2.01	2.28	2.30
7	1.92	2.04	1.81	1.98	2.00
8	1.76	1.88	1.67	1.79	1.80



(a)



(b)

Fig. 7. (a) Macroscopic stress–strain response by plane strain and plane stress VCFEM simulation. (b) Stress–strain hardening rate plots for the Considere condition.

Table 4. Comparison of the number of cracked particles obtained by Weibull based VCFEM simulation with experimental observations

Section #	Exp.	$\sigma_0 = 3.01$	$\sigma_0 = 3.04$	$\sigma_0 = 3.19$	$\sigma_0 = 2.79$
1	33	34	30	24	39
3	33	29	29	20	36
5	29	26	28	25	34
9	24	28	27	26	30

The Weibull parameters are also calibrated using a three-dimensional ABAQUS model simulation of a cubic unit cell with a single, 15% volume fraction, spherical particle as described in Ref. [24]. The  $1 \times 1 \times 1$  unit cell model has a particle of radius  $R = 0.66$ . A modified form of equation (5) is used to account for the shape variability of the particles as

$$\rho(\alpha, v) = \int_{\alpha_{\min}}^{\alpha_{\max}} \int_{V_{\min}}^{V_{\max}} p(\alpha)p(v)P_f(v, \sigma_1) dv \quad (6)$$

where  $\alpha$  corresponds to the particle aspect ratio. The particle size and shape distribution functions  $p(v)$  and  $p(\alpha)$  are calculated from the computer simulated representation of the actual three-dimensional microstructure shown in Fig. 3. This average particle volume and the fraction of cracked particle are directly computed from Fig. 3 as  $\bar{v} = 642.0 \mu\text{m}^3$  and  $\rho = 45.48\%$ . The average particle stress at a macroscopic strain  $\epsilon = 8.88\%$  is obtained from the ABAQUS simulation as  $\sigma_p = 862.60$  MPa. Results of calibration with and without shape effects are documented in Table 3. It is found that the best agreement in  $\sigma_0$  for all two-dimensional sections and three dimensions is obtained for  $m$  between 4 and 5. Consequently the parameter is chosen to be  $m = 4.2$ . The corresponding value of  $\sigma_0$  for section 2 is 3.04 GPa, for section 8 is 3.19 GPa, for section 14 is 2.79 GPa and the average of these sections is  $\sigma_0 = 3.01$  GPa.

Results of VCFEM analysis of the simulated micrographs of sections 1, 3, 5 and 9 are provided in Table 4. The number of cracked particles at a macroscopic strain of 8.88% by VCFEM are compared with experimental results. While the general agreement is quite good, it is seen that the concurrence is particularly favorable when the simulation is conducted with a  $\sigma_0$  that is obtained from a section that is near to the one being analyzed. For example, the results of sections 1 and 3 are very good when  $\sigma_0 = 3.01$  GPa, which is obtained from section 2. This concurrence may be attributed to the similarity in the distribution of heterogeneities in neighboring sections, and suggests that spatial distribution has a strong effect on the Weibull parameters.

*5.1.1. Microscopic damage analysis.* Various results for section 1 which contain a dominant damage path are generated by VCFEM simulation and compared with experimental observations in this section. The macroscopic stress–strain plot for

plane strain and plane stress assumptions are compared with experimental results in Fig. 7(a). The overall yield strength is better predicted by the plane stress model. However, the post yield behavior with plane strain conditions is much closer to the experimental results. The initial higher yield strength is expected with plane strain due to the plastic constraint caused by the  $\epsilon_z = 0$  condition. A shifted stress–strain plot [modified plane strain VCFEM result in Fig. 7(a)] where the stresses are reduced by the initial difference in yield stress shows a very good match between experiments and simulation. Thus plane strain assumptions are used in subsequent computations. Figure 7(b) is intended to predict the onset of plastic instability by the model and compare it with the actual fracture observed in the experiments. The use of the Considere criterion to predict the onset of plastic instability has been suggested by Llorca and Gonzalez [2, 34] in the absence of dilatational strain associated with reinforcement fracture. In this criterion, the average stress  $\bar{\sigma}$  is related to the strain hardening rate  $d\bar{\sigma}/d\epsilon$  as

$$\bar{\sigma} = \frac{d\bar{\sigma}}{d\epsilon}. \quad (7)$$

The strain derived from this relation corresponds to the lower bound of the tensile ductility since it controls the composite load bearing capacity. Three sets of curves are plotted in Fig. 7(b) corresponding to the matrix material, the VCFEM results in plane strain and the experimental results. It is seen that the Considere criterion (junction of the two curves) predicts the experimental point corresponding to the onset of fracture rather well. Additionally the two-dimensional prediction of the plane strain simulation is also quite good and can be used with reasonable confidence.

Microstructural results of the simulation are compared with experiments in Figs 8. The computed micrograph with evolved damage for section 1 is compared with the experimental micrograph at 8.88% strain in Figs 8(a) and (b). The damaged particles are shown with the contained crack. Most damaged particles in the simulation coincide with the experimental results, with the box indicating the dominant damage path. The damage path is approximately perpendicular to the tensile loading direction. Figure 8(b) also shows the contour plot of effective plastic strain in the ductile matrix and indicates the path of damage linkage. The plastic strain is higher and localized between cracked par-

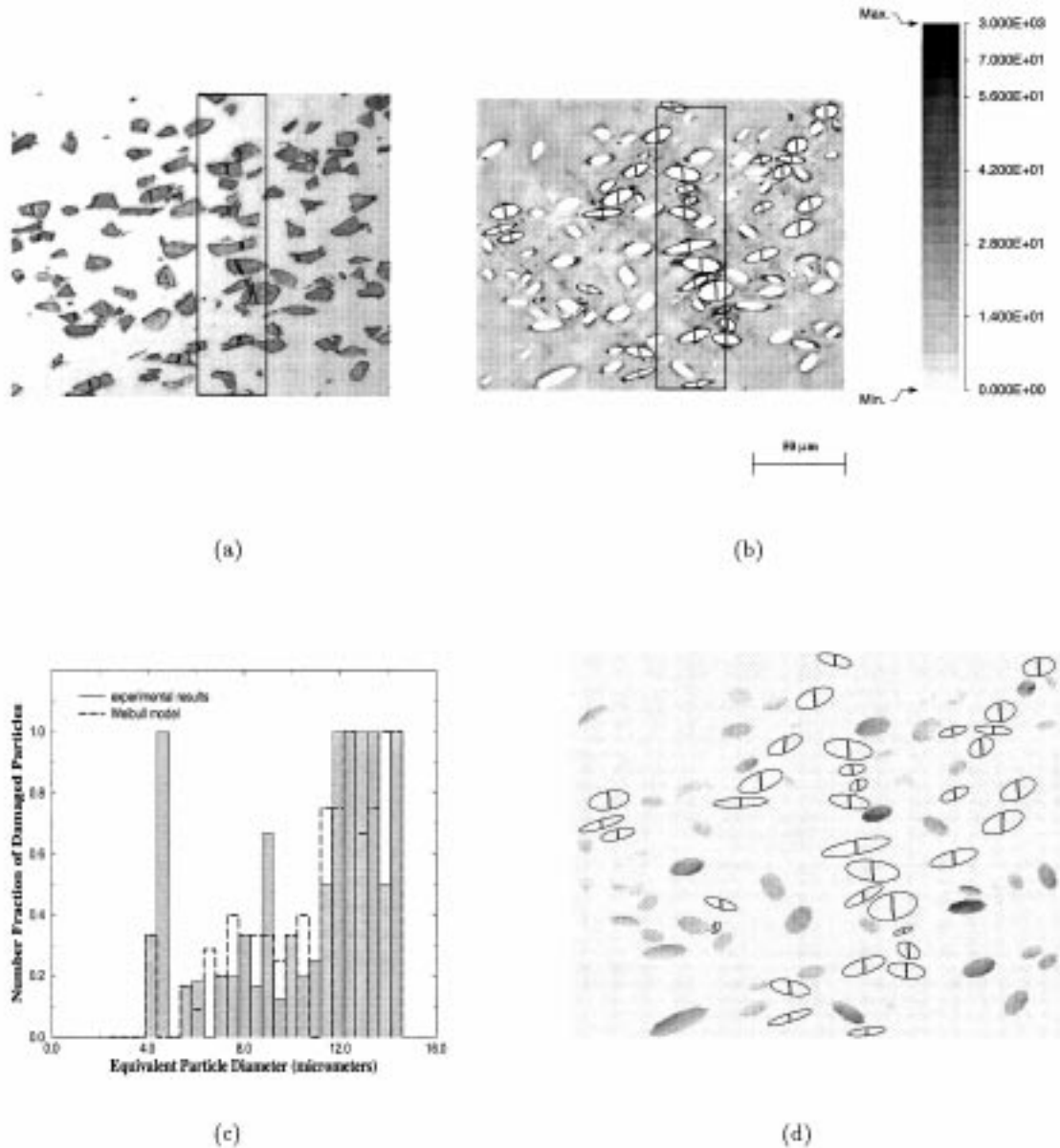


Fig. 8. (a) Experimental micrographs, (b) VCFEM simulated micrograph showing damage and contour plot of effective plastic strain at 8.88% strain in section 1, (c) histogram of number fraction of cracked particles as a function of particle size by Weibull based probabilistic criterion, and (d) contour plot of particle fracture probability of section 1 at 8.88% strain.

ticles and this is expected to cause matrix cracking. The number fraction of cracked particles in different size ranges is plotted in Fig. 8(c). Very good agreement is seen between simulation and experimental results. Figure 8(d) is a contour plot of the particle fracture probability at 8.88% strain. The black shade corresponds to the highest probability and fractured particles are illustrated in white with a crack. Similar plots (not shown) at earlier stages of deformation show that several particles with higher probability at the smaller strain have cracked with deformation. The number fractions of cracked

particles as a function of straining are plotted for sections 1, 5 and 9 together with the experimental observation in Fig. 9. At lower strains the number fractions of cracked particles for sections 1 and 5 with particle rich regions are higher than that for section 9. This is due to higher stress concentration particle rich areas that are enough to fracture some particles even at low strains. With increasing strains more particles start to crack in section 9 and exceeds that for section 5 which has less particles in the clustered regions. The two-dimensional simulations however exhibit less cracked particles

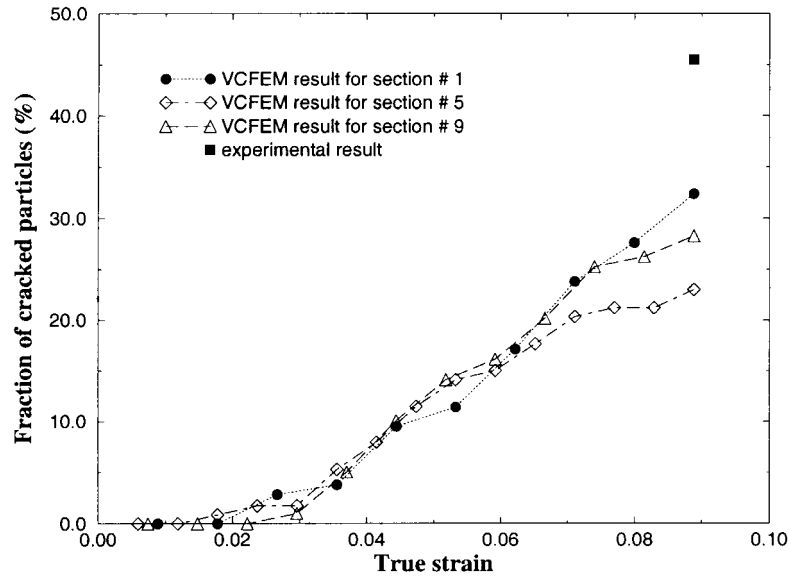


Fig. 9. Number fraction of cracked particles as a function of straining.

than that in the actual three-dimensional microstructure.

### 6. CHARACTERISTIC SIZE OF MICROSTRUCTURES

The influence region of local morphology on the mechanical response is characterized by a microstructural representative material element (RME) that is critical in delineating length scales. The RME depicts a region which is assumed to be representative of the entire microstructure. Functions that distinguish between variations in stress/strain distributions for local disturbances in microstructural patterns can provide important insight on microstructure–property relations. Marked correlation functions, discussed in Refs [10, 21, 24, 33] for multivariate characterization of patterns, are evaluated to characterize length scales or RME size in the presence of damage. A

mark may be identified with an appropriate microstructural variable, e.g. in this case a variable that is related to quantification of damage. The marked correlation function for a heterogeneous domain  $W$  of volume  $V$  containing  $N$  heterogeneities is mathematically expressed as [10, 21, 22]

$$M(r) = \frac{\left[ \frac{dH(r)}{dr} \right]}{g(r)} / (4\pi r^2);$$

$$H(r) = \frac{1}{m^2} \frac{V}{N^2} \sum_{i=1}^N \sum_{k=1}^{k^i} m_i m_k(r) \quad \text{and} \quad (8)$$

$$g(r) = \frac{1}{4\pi r^2} \frac{dK(r)}{dr}$$

where  $K(r)$  is the second order intensity function defined in Refs [31, 33],  $g(r)$  is the pair distribution function and  $H(r)$  is the mark intensity function.

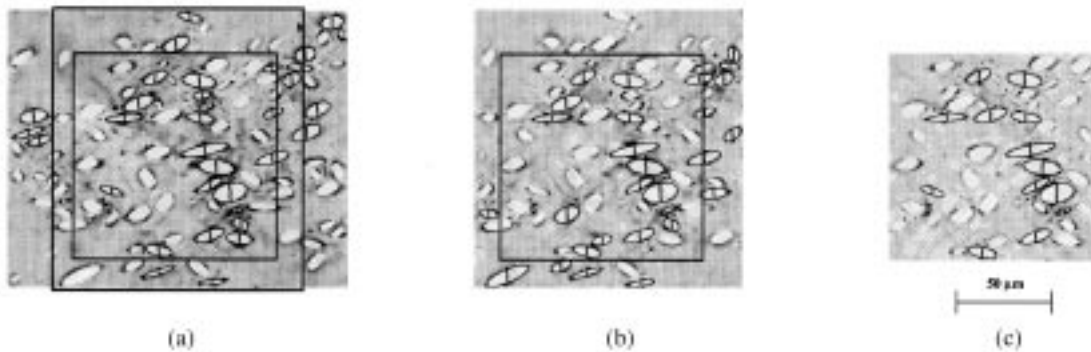


Fig. 10. Simulations showing effective plastic strain (%) and cracked particles in three different subsets of the entire micrograph of section 1: (a) RME 0 with dimension  $195 \times 155 \mu\text{m}^2$ ; (b) RME 1 with dimension  $150 \times 155 \mu\text{m}^2$ ; (c) RME 2 with dimension  $116 \times 115 \mu\text{m}^2$ .

The  $H(r)$  function reduces to the  $K(r)$  function if all heterogeneities have the same mark. A mark associated with the  $i$ th heterogeneity is denoted as  $m_i$ ,  $k^i$  is the number of heterogeneities which have their centers within a sphere of radius  $r$  around the  $i$ th heterogeneity, for which the mark is  $m_k$ , and  $m$  is the mean of all marks. By definition  $M(r)$  estab-

lishes a relation between the location and associated variables for heterogeneities. Two marks are considered in this study. The first corresponds to particle cracks and are designated as  $m_i = 1$  for a cracked particle and  $m_i = 2$  for an intact particle. The second corresponds to the probability of particle fracture, which signifies the propensity to

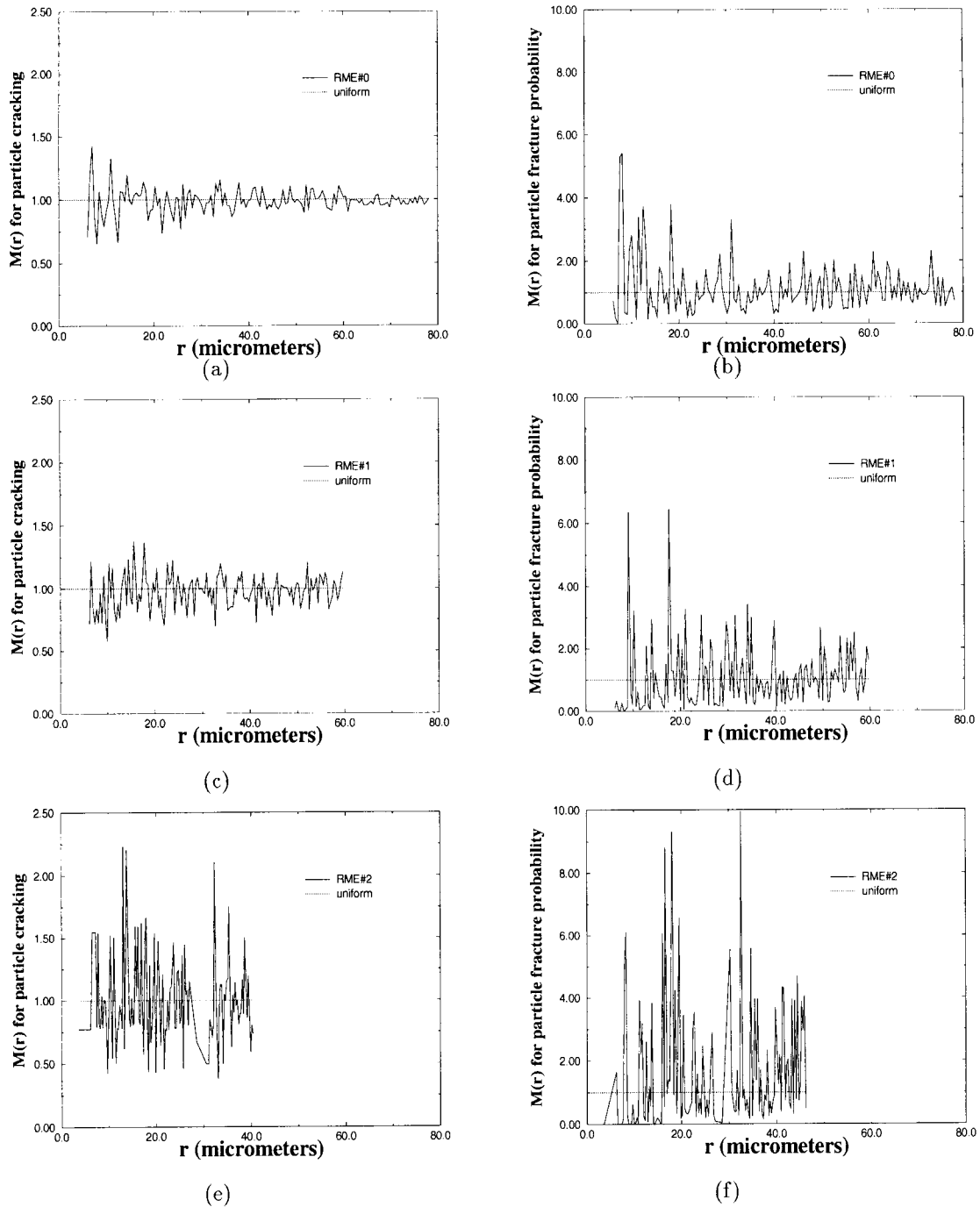


Fig. 11. Marked correlation function as a function of radial distance: (a) cracked particles as marks; (b) probability of cracking as mark for RME 0; (c) cracked particles as marks; (d) probability of cracking as mark for RME 1; (e) cracked particles as marks; (f) probability of cracking as mark for RME 2.

advance the microstructural damage state. The  $M(r)$  function statistically stabilizes at near-unit values at a distance  $r_{\text{inter}}$  at which the local morphology ceases to have any significant influence on an evolving variable. Values of  $M(r) > 1$  show positive correlation, while  $M(r) < 1$  indicates repulsion between marks. This distance  $r_{\text{inter}}$  is an indication of the physical range of interaction and is significant in making decisions about length scales and the RME size.

The marked correlation functions corresponding to cracked particles and probability of fracture, are plotted in Figs 11(a) and (b) from the simulation of the entire micrograph of section 1 (termed as RME 0) with dimensions  $195 \times 155 \mu\text{m}^2$ . The dotted line corresponds to the unit  $M(r)$  for uniform distribution of spherical heterogeneities with identical marks. Contour plots of the equivalent plastic strain in the simulated micrograph with cracked particles are shown in Fig. 10(a). The particle area fraction for this micrograph is 18.37% and the total number of particles and cracked particles are 105 and 34, respectively. The plots are made with only up to 40% of the entire micrograph, or  $80 \mu\text{m}$  to avoid boundary effects in  $M(r)$ . The  $M(r)$  functions in both figures approximately stabilize at near-unit values at a distance  $r_{\text{inter}}$  of about  $60 \mu\text{m}$ . At this distance, the local morphology is expected to have a significantly reduced influence on the evolving variables. The slower attenuation of  $M(r)$  for particle fracture at shorter range indicates the strong effect of the local morphology on damage evolution. Next, a smaller region (RME 1) is selected for damage simulation corresponding to the stabilized region in the  $M(r)$  plots. Since the stable region is  $60 \mu\text{m}$ , the dimension of the micrograph is chosen to be  $150 \times 155 \mu\text{m}^2$ , incorporating the scaling factor, i.e.  $60/0.4 = 150$ . This is shown with the box in Fig. 10(a). Again the contour plots of plastic strain with cracked particles by VCFEM simulation are shown in Fig. 10(b). The dominant crack behavior is quite similar to that for RME 0, even though there is some difference near the boundary. Also the plastic strain contours and limiting values are similar. The particle area fraction for RME 1 is 18.13% with the total number of particles and cracked particles at 84 and 28, respectively. The  $M(r)$  plots in Figs 11(c) and (d) show that the functions may still be assumed to stabilize at around  $60 \mu\text{m}$ . A smaller subset (RME 2), with dimensions  $116 \times 115 \mu\text{m}^2$  is next simulated and the plastic strain is depicted in Fig. 10(c). Significantly different plastic strains and cracking pattern are observed for this microstructure. The particle area fraction for this micrograph is 18.68% with a total of 51 particles of which 18 are cracked. The plots of  $M(r)$  function do not stabilize in the domain of the simulation window. Through this analysis the size effect of microstructure, needed for adequate represen-

tation and analysis in the presence of evolving damage is demonstrated.

## 7. CONCLUSIONS

In this paper, a combination of experimental and computational methods are utilized to characterize and understand the evolution of microscopic damage that causes failure in naturally aged commercial SiC particle reinforced DRAs. The main mode of damage for the naturally aged material is found to be particle cracking. Larger particles in particle rich regions are more susceptible to cracking than those in particle sparse regions. Spatial distribution of particles plays a more important role in damage than particle size for this material. A sensitivity analysis with respect to microstructural parameters infers that the strongest influence on particle cracking comes from the size and local spatial distribution. Particle shape, orientation and nearest neighbor orientation have relatively smaller effects on damage initiation. Histograms of particles forming the dominant damage path in comparison with all cracked particles reveal that larger particles oriented in the loading direction and in relatively rich areas are more susceptible to contribute to a dominant crack in the microstructure. In an attempt to identify discriminating characteristics of two-dimensional micrographs that may be of help in making dominant damage predictions for the actual three-dimensional microstructures, probability density functions of particle size, nearest neighbor distance, and second order intensity function  $K(r)$  of spatial distribution are plotted. Better representation of damage is possible with those sections that have higher peaks at lower nearest neighbor distances and longer tails, as well as a propensity towards clustering.

Next the two-dimensional Voronoi cell finite element model is used to simulate microstructural damage evolution in computer generated equivalent micrographs. Both macroscopic and microscopic variables obtained by the VCFEM simulation are compared with experimental observations. The macroscopic stress-strain plot for the plane strain analysis is found to yield quite good match with experiments if the difference in the initial yield strength due to plastic constraint is subtracted. Prediction of the onset of plastic instability by the Considere criterion is also found to be in reasonably good agreement with the experimental results. For the microstructural results with a number of cracked particles in different size ranges, the Weibull model is found to give better concurrence with experiments. A plot of the number fraction of cracked particles as a function of straining shows that at lower strains sections with particle rich regions damage rapidly, but the rate slows down with additional deformation. Finally, the marked correlation functions are evaluated to characterize

length scales and representative material element size in the presence of damage. Particle cracks and the probability of particle fracture are chosen to be the marks. The study reveals that a significantly large portion of the microstructure should be analyzed for reasonable accuracy in the presence of damage. The correlation functions do not stabilize below a certain length scale and this keeps growing with increased damage. In summary, various important characteristics of growing damage are investigated in this work in order to understand the role of microstructure in the material failure process.

*Acknowledgements*—The authors would like to thank H. Weiland, T. R. Rouns, W. H. Hunt and R. Brasil of ALCOA Technical Center for their help on the experimental portion of this work. The authors are grateful to S. Moorthy for his help with the VCFEM simulations and discussions on modeling. This work has been sponsored by the Mechanics and Materials program (Program Director S. Saigal) of National Science Foundation through a NSF Young Investigator grant (Grant No. CMS-9457603), by the United States Air Force Office of Scientific Research through grant No. F49620-98-1-01-93 (Program Director: Ozden O. Ochoa) and by the United States Army Research Office through grant No. DAAH04-95-1-0176 (Program Director: K. R. Iyer). Computer support by the Ohio Supercomputer Center through grant # PAS813-2 is also gratefully acknowledged.

#### REFERENCES

- Singh, P.M. and Lewandowski, J.J., *Metall. Trans. A*, 1995, **26A**, 2911.
- Llorca, J. and Gonzalez, C., *J. Mech. Phys. Solids*, 1998, **46**, 1.
- Pandey, A. B., Majumdar, B. S. and Miracle, D. B., *Processing and Fabrication of Advanced Materials, Proc. of TMS Conf.*, ed. T. S. Srivatsan and J. J. Moore, 1995, p. 185.
- Mummery, P.M., Derby, B. and Scruby, C.B., *Acta metall. mater.*, 1993, **41**, 1431.
- Brechet, Y., Embury, J.D., Tao, S. and Luo, L., *Acta metall. mater.*, 1993, **39**, 1781.
- SPYGLASS Slicer, Quick Tour and Reference*, Version 1.0. Spyglass Inc., Champaign, IL 61826, U.S.A., 1994.
- Hunt, W. H., Ph.D. thesis, Carnegie Mellon University, 1992.
- Llorca, J. and Elices, M., *Intrinsic and Extrinsic Fracture Mechanisms in Inorganic Composite Systems*, ed. J. J. Lewandowski and W. H. Hunt. Minerals, Metals and Materials Society, Warrendale, PA, 1995, p. 15.
- Christman, T., Needleman, A. and Suresh, S., *Acta metall. mater.*, 1989, **37**, 3029.
- Moorthy, S. and Ghosh, S., *Comp. Meth. Appl. Mech. Engng*, 1998, **151**, 377.
- Ghosh, S. and Moorthy, S., *Acta metall. mater.*, 1998, **46**, 965.
- Needleman, A., *J. appl. Mech.*, 1987, **54**, 525.
- Tvergaard, V., *J. Mech. Phys. Solids*, 1991, **41**, 1309.
- Bao, G., *Acta metall. mater.*, 1992, **40**, 2547.
- Hom, C.L., Mataga, P.A. and McMeeking, R.M., *Int. J. Numer. Meth. Engng*, 1989, **27**, 233.
- Finot, M., Shen, Y.-L., Needleman, A. and Suresh, S., *Metall. Mater. Trans. A*, 1994, **25A**, 2403.
- Brockenbrough, J.R., Suresh, S. and Weinecke, W.A., *Acta metall. mater.*, 1991, **39**, 735.
- Brockenbrough, J.R., Hunt, W.H. Jr and Richmond, O., *Scripta metall.*, 1992, **27**, 385.
- Becker, R. and Richmond, O., *Model. Simul. Mater. Sci. Engng*, 1994, **2**, 439.
- Spitzig, W.A., Kelly, J.F. and Richmond, O., *Metallography*, 1985, **18**, 235.
- Wray, P.J., Richmond, O. and Morrison, H.L., *Metallography*, 1983, **16**, 39.
- Pyrz, R. and Bochenek, B., *Sci. Engng Comp. Mater.*, 1994, **3**, 95.
- Li, M., Ghosh, S., Rouns, T.N., Weiland, H., Richmond, O. and Hunt, W., *Mater. Characterization*, 1998, **41(2/3)**, 81.
- Li, M., Ghosh, S., Richmond, O., Weiland, H. and Rouns, T. N., *Mater. Sci. Engng A*, 1999, **A265**, 153.
- Li, M., Ghosh, S., Richmond, O., Weiland, H. and Rouns, T. N., *Mater. Sci. Engng A*, 1999, **A266**, 221.
- Hunt, W. H., *Intrinsic and Extrinsic Fracture Mechanisms in Inorganic Composite Systems*, ed. J. J. Lewandowski and W. H. Hunt. Minerals, Metals and Materials Society, Warrendale, PA, 1995, p. 31.
- Lewandowski, J. J., Liu, C. and Hunt Jr, W. H., in *Powder Metallurgy Composites*, ed. P. Kumar, K. M. Vedula and A. M. Ritter. TMS-AIME, Warrendale, PA, 1987, p. 117.
- Lloyd, D.J., *Acta metall. mater.*, 1991, **39**, 59.
- Rokhlin, S.I., Huang, W. and Chu, Y.C., *Ultrasonics*, 1995, **33**, 351.
- Potet, P., Bathias, C. and Degriigny, B., *Mater. Eval.*, 1988, **46**, 1050.
- Buffiere, J.-Y., Maire, E., Verdu, C., Cloetens, P., Pateyron, M., Peix, G. and Baruchel, J., *Mater. Sci. Engng*, 1997, **A234-236**, 633.
- Pyrz, R., *Mater. Sci. Engng*, 1994, **A177**, 253.
- Ghosh, S., Nowak, Z. and Lee, K., *Acta mater.*, 1997, **45**, 2215.
- Gonzalez, C. and Llorca, J., *Scripta mater.*, 1996, **35**, 91.
- Ghosh, S., Nowak, Z. and Lee, K., *Comp. Sci. Technol.*, 1997, **57**, 1187.
- Hunt, W.H. Jr, Osman, T.M. and Lewandowski, J.J., *JOM*, 1993, **45(1)**, 30.
- Singh, P. M. and Lewandowski, J. J., in *Intrinsic and Extrinsic Fracture Mechanisms in Inorganic Composite Systems*, ed. J. J. Lewandowski and W. H. Hunt. Minerals, Metals and Materials Society, Warrendale, PA, 1995, p. 57.
- Hunt, W. H., Cook, C. R. and Sawtell, R. R., SAE Paper, 910834, 1991.
- Llorca, J., *Acta metall. mater.*, 1995, **43**, 181.